Boosting excitons dissociation in defective-rich graphitic carbon nitride for efficient hydrogen peroxide photosynthesis and on-site environmental governance

Longhui Zheng [a,*], Zhiying Wang [a], Haobo Zhang [a], Yanbiao Shi [b,c,**], Fanyu Wang [c], Zhongsen Wang [c], Di Lin [a], Jiahui Yue [a], Qizhao Wang [d,e,***]

[a] College of Forestry, Henan Agricultural University, Zhengzhou 450002, PR China
[b] School of Environmental Science and Engineering, Shanghai Jiao Tong University, Shanghai 200240, PR China
[c] Key Laboratory of Pesticide & Chemical Biology of Ministry of Education, Institute of Environmental & Applied Chemistry, College of Chemistry, Central China Normal University, Wuhan 430079, PR China
[d] School of Water and Environment, Key Laboratory of Subsurface Hydrology and Ecological Effects in Arid Region of Ministry of Education, Chang'an University, Xi'an 710054, PR China
[e] College of Chemistry and Chemical Engineering, Northwest Normal University, Lanzhou 730070, PR China

A R T I C L E   I N F O

A B S T R A C T

Solar-driven hydrogen peroxide (H_2O_2) production offers a sustainable strategy to address the ever-growing demand of eco-friendly oxidant and clean fuel, while its efficiency highly relies on the generation of desired reactive oxygen species (ROSs). Herein, we demonstrate that introducing boron-nitrogen vacancy (B-N_V) associates in g-C_3N_4 enables to weaken the robust excitonic effect and promote bound excitons spontaneously dissociating into free charge carriers under ambient conditions. Specifically, the doped B atoms introduced a donor state below the conduction band of g-C_3N_4, which disturbs charge distribution around heptazine rings and further destabilizes excitons. The concomitant N_V, serving as an accepter state locating above the valence band, cooperates with the doped B atoms to form B-N_V associates that simultaneously downshifts the conduction band and valence band of g-C_3N_4. Distinct from the counterpart preferring to activate O_2 into $^1O_2$ via an energy-transfer-involved pathway, g-C_3N_4 featuring with B-N_V associates displayed a superior photoactivity of visible-light-driven two-electron oxygen reduction reaction for H_2O_2 production with a yield of 182 μmol h^{-1} and selectivity of 100%. The produced H_2O_2 could effectively degrade organic contaminants and kill typical bacteria. This study highlights the importance of ROSs generation in two-dimensional photocatalysts for sustainable solar-to-chemical conversion and *on site* environmental governance.

1. Introduction

H_2O_2 is a green ready-to-use oxidant in wastewater purification, sterilization, leaching, and clean fuel for jet car and rocket. Nowadays, industrial H_2O_2 production highly depends on the indirect anthraquinone oxidation, alcohol oxidation or direct synthesis from H_2 and O_2, which, however, is a waste-intensive, energy-consuming and easily explosive process [1–3]. Solar-driven H_2O_2 production from ubiquitous oxygen or water catalyzed by earth-abundant semiconductors has been regarded as a promising strategy owing to its safe, sustainable, cost-effective, energy-saving and environmentally benign nature [4,5]. Under solar light irradiation, photoelectrons prefer to activate O_2 into H_2O_2 via a successive two-electron oxygen reduction reaction [$2e^-$ ORR, Eq. (1)] [6,7], while photoholes intend to oxidize the absorbed H_2O or bound hydroxyl (−OH) on catalysts' surface into H_2O_2 through a two-electron water oxidation reaction [$2e^-$ WOR, Eqs. (2–3)] [8,9]. However, the current state-of-art artificial H_2O_2 photosynthesis catalysts are still far from efficiency due to the low production rates of

desired ROSs and competitive side-reactions.

$$O_2 + 2H^+ + 2e^- \rightarrow H_2O_2 \tag{1}$$

$$2H_2O + 2h^+ \rightarrow H_2O_2 + 2H^+ \tag{2}$$

$$2OH^- + 2h^+ \rightarrow H_2O_2 \tag{3}$$

The preferred alternative for high-efficiency H_2O_2 photosynthesis is to boost the selective production of desired ROSs and inhibit the unwanted side-reactions. For instance, photocatalytic H_2O_2 production via the $2e^-$ ORR process is closely related to the formation of superoxide radical ($\bullet O_2^-$), which is governed by the conduction band (CB) of photocatalysts [10,11]. Therefore, the prerequisite condition for semiconductor-based photocatalyst with efficient $\bullet O_2^-$ generation is their CB negative than the reduction potential of O_2 toward $\bullet O_2^-$ [Eq. (4)] [12–16]. However, the conversion of $\bullet O_2^-$ to H_2O_2 is not a trouble-free journey because the newly formed $\bullet O_2^-$ might be consumed by the dissolved organic matters or oxidized by holes [Eq. (5)], resulting in an insufficient energy conversion of solar-to-H_2O_2 [17,18]. As for the $2e^-$ WOR pathway, H_2O_2 was produced along with the oxidation of bound H_2O/OH^- on photocatalyst's surface by holes. This process can overcome the limitation of mass transfer over photocatalysts' surface because the $2e^-$ WOR-involved H_2O_2 production only requires water as the source rather than the dissolved O_2 [19]. Frustratingly, the $2e^-$ WOR pathway for H_2O_2 production suffers from a larger energy per electron to initiate the chemical reactions, which is a thermodynamically unfavorable process when compared with the $4e^-$ WOR [20,21]. Besides, the accumulated H_2O_2 over photocatalysts' surface might serve as hole scavenger that was decomposed into O_2 [Eq. (6)] [22]. To address all these drawbacks of artificial H_2O_2 production, a compromised approach is to develop a paradigmatic photocatalyst that features with the superior $2e^-$ ORR photoactivity and simultaneously substitutes the thermodynamically unfavorable $2e^-$ WOR process with a more progressive oxidative reaction [23–25].

$$O_2 + e^- \rightarrow \bullet O_2^-, \; E_0 = -0.33 \; V_{NHE} \tag{4}$$

$$\bullet O_2^- + h^+ \rightarrow {}^1O_2, \; E_0 = +0.34 \; V_{NHE} \tag{5}$$

$$H_2O_2 + 2h^+ \rightarrow 2H^+ + O_2 \tag{6}$$

Two-dimensional (2D) layered photocatalysts (g-C_3N_4, MoS_2, BiOX (X = Cl, Br, I), *i*COF DBTP [26–29], perylenetetracarboxylic acid [30] have been deemed as a universal and feasible platform to realize the $2e^-$ ORR-driven H_2O_2 photosynthesis due to the abundant surface reactive sites, short charge carriers transport path, improved conductivity and adjustable electron configuration [17,31,32]. Unfortunately, the limited spatial dimensionality of 2D layered photocatalysts bears with the reinforced interlayer Coulomb interactions, resulting in photoexcited electron-hole pairs to be bound as the electroneutral singlet excitons (S_1, $e^- - h^+$) rather than completely separated into free charge carriers [33]. Undergoing an intersystem crossing (ISC), singlet excitons transforms into triplet excitons (T_1) accompanied by the activation of triplet O_2 (${}^3\sum_g^-$) into singlet ${}^1O_2$ (${}^1\Delta_g$) via an excitonic energy transfer process [34]. Unlike the charge carrier-involved radical or anionic ROSs ($\bullet O_2^-$ and O_2^{2-}), the generation of ${}^1O_2$ is adverse to the $2e^-$ ORR-driven H_2O_2 photosynthesis. In this regard, it is of great significance to weaken the robust excitonic effects of 2D layered photocatalysts toward facilitating exciton dissociation into charge carriers. Several strategies have been proposed to boost charge carriers' generation in 2D layered photocatalysts under ambient conditions, including defects engineering [35], extraneous element doping [36–38], designing highly-exposed van der Waals gaps [39], constructing order-disorder interfaces [40,41], surface modification with inorganic oxyanions [33,42], and loading molecular co-catalysts [43]. However, modulating the excitonic effect of 2D layered photocatalysts by introducing the defects, heteroatoms or van der Waals gaps fails to overall optimize the band structure or even upraise the valence band (VB) position, leading to the insufficient driving

force of VB to trigger water oxidation reaction. While the formation of interfacial junction caused by local disordering or surface inorganic oxyanion-modified layer is often persecuted by the weakened reduction potential of photocatalysts.

Herein, boron dopant was subtly introduced into g-C_3N_4 framework, a superior visible-light-response polymeric semiconductor, via our previously developed B_2O_3 molten salt method [35]. Based on the theoretical calculation and experimental analysis, the excitonic effect of g-C_3N_4 was weakened by introducing a defect level of B doping, which disturbs the charge distribution around heptazine rings and induces excitons dissociation into charge carriers. While the doped B preferentially substituted the carbon atoms of triazine ring, leading to the cleavage of C-N-C bonds and formation of intimate B-N_V associate. Under the optimal conditions, this elaborate B-N_V associate displayed a superior $2e^-$ ORR-driven photoactivity for H_2O_2 production in isopropanol solution with a rate of 182 μmol h^{-1}, approximately 4.2 times higher than that in pure water. This study highlights the importance of manipulating excitonic effect of 2D layered semiconductors for charge-carrier-involved photocatalysis and provides a sustainable strategy for the solar-driven green production of ready-to-use oxidant.

2. Experimental section

2.1. Synthesis of photocatalyst

Bulk g-C_3N_4 was synthesized via a typical thermo-polymerization process. The melamine superfine powder (10 g) was directly heated to 550 °C with a heating rate of 2.5 °C min^{-1} and kept for 4 h in air [43].

Homogeneous B doped g-C_3N_4 was synthesized according to our previously developed B_2O_3 molten method. Briefly, 1 g of bulk g-C_3N_4 was mixed with B_2O_3 (2.5 g) and ground for 0.5 h. The obtained mixture was spread in a silica crucible and heated to 360 °C for 2h with a heating rate of 5 °C min^{-1} in N_2 atmosphere. The collected yellow solid was dispersed into hot oxygen-free water to remove the residual B_2O_3. The precipitate was washed with ethanol for several times and dried in air at 60 °C overnight. The as-prepared g-C_3N_4 with different B contents was synthesized through the same process with the dosage of B_2O_3, which were donated as CN-N_V-x (x = 1.5, 2, 2.5 and 3).

2.2. Photocatalytic H_2O_2 production

Photocatalytic H_2O_2 production was carried out in a quartz photoreactor with a 300 W Xe lamp (λ > 420 nm, Microsolar300, Beijing Perfectlight) as light source. The sample (30 mg) was dispersed into isopropanol solution (IPA, 3 vol%, 30 mL). The suspension was ultrasonically treated for 5 min and purged with O_2 (50 mL/min). The pH of initial solution was adjusted with 0.1 mol/L NaOH or $HClO_4$ solution. H_2O_2 concentration was quantificationally measured by a modified DPD-POD method. 1 mL of solution was taken at a predetermined interval and filtered through filter membrane (0.22 μm).

2.3. On site utilization of H_2O_2

The potential of on site produced H_2O_2 for wastewater treatment and sterilization was carried out under ambient conditions. Para-chloronitrobenzene (4-NP), rhodamine B (RhB), tetracycline (TC), bisphenol A (BPA) and 4-chlorophenol (4-CP) were selected as the representatives of organic contaminants, respectively. Escherichia coli was regraded as the model bacteria in drinking water. Typically, the produced H_2O_2 (10 mL) was added into 40 mL (5 mg L^{-1}) of 4-NP, RhB, TC, BPA or 4-CP solution. A 300 W Xe lamp with visible light cut-off filter (300 nm < λ < 400 nm) was used as ultraviolet light source. 1 mL of solution was extracted and filtered after a constant interval. The concentration of 4-NP, RhB, TC, BPA or 4-CP was quantitatively analyzed by ultraviolet spectrophotometer. The sterilization experiment was proceeded by adding 10 mL the produced H_2O_2 into Escherichia coli
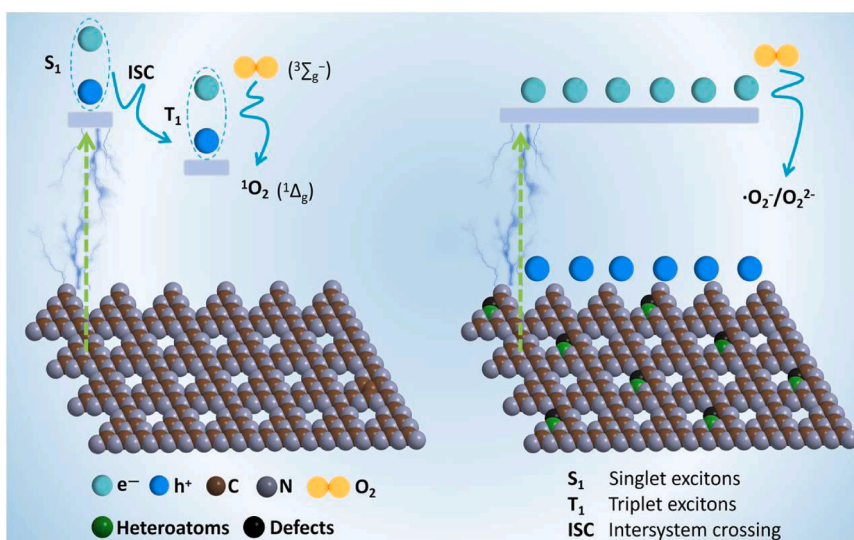
Scheme 1. Schematic illustration of exciton- and charge carrier- transfer involved photocatalytic O$_2$ activation. (Left) Formation of excitons and their intersystem crossing from S$_1$ to T$_1$. (Right) Generation of electrons and holes, and the subsequent charge-carrier transfer involved O$_2$ activation.

solution. The sterilization efficiency was calculated through the plate count method. For comparison, the control groups for organic contaminant degradation and sterilization were also conducted in dark with the presence of H$_2$O$_2$ and catalysts.

3. Results and discussion

g-C$_3$N$_4$ showcases immense potentials in green energy production and environmental contaminant control. However, pristine g-C$_3$N$_4$ photocatalyst suffers from poor charge carrier separation efficiency and insufficient surface reactive sites. To circumvent the limitation of sluggish charge carrier kinetics, reducing the dimensionality of g-C$_3$N$_4$ enables to shorten the diffusion distance of photo-excited charge carriers from the bulk to the surface. While increasing the surface area and engineering the surface atomic arrangement could provide enough reactive sites, thus accelerating catalytic reactions. All these merits of 2D g-C$_3$N$_4$ inspire us to develop efficient catalysts for artificial H$_2$O$_2$ photosynthesis. Our previous work has demonstrated that molten B$_2$O$_3$ could simultaneously serve as the molten medium and doping precursor to synthesize homogeneously B-doped photocatalysts [35]. In this case, pristine g-C$_3$N$_4$, obtained from the calcination of melamine in air, was ground with crystalline B$_2$O$_3$ and then heated in a tube furnace in N$_2$ atmosphere (Fig. 1a). Driven by the strong space confinement effect, the molten B precursor would intercalate into the interlayer of g-C$_3$N$_4$ nanosheets and substitute the host atoms. Nitrogen vacancy (N$_V$), a common anion defect existing in nitrides, might be introduced into the g-C$_3$N$_4$ framework along with the breaking of hydrogen bonds of polymeric melon units and the thermal-driven releasing of −NH$_2$ group [44]. The residual B$_2$O$_3$ was washed off by dispersing the sample into hot oxygen-free water. The final product containing both doped B atoms and N$_V$ was donated as CN-B-N$_V$. Scanning electron microscopy (SEM) and transmission electron microscopy (TEM) images suggested that the obtained CN-B-N$_V$ nanosheets still kept its pristine lamellar structure without obvious destruction (Fig. 1b and S1-S2). Elements mapping manifested that the doped B atoms homogeneously disperses in the CN-B-N$_V$ nanosheet (Fig. 1c-f). The selected area electron diffraction (SAED) pattern obtained from high-resolution TEM (HRTEM) images showcased the clear lattice fringe (d = 0.336 nm) of the (002) atomic planes of g-C$_3$N$_4$ (Fig. 1g). Compared with pristine g-C$_3$N$_4$ (CN), CN-B-N$_V$ nanosheet showed a prominent shift of (002) diffraction peak to higher 2θ angles owing to the presence of anisotropic microstrain, suggesting that B atoms was successfully doped into the g-C$_3$N$_4$

framework (Fig. 1h). This result corresponds to the result obtained from Fourier transform infrared spectroscopy (FTIR) and Raman spectra (Fig. S3). The B-doping-induced increase of the specific surface area of g-C$_3$N$_4$ was further revealed by N$_2$ adsorption and desorption isothermal curves (Fig. S4). The specific surface area of CN-B-N$_V$ was about 24.47 m^2/g, which is larger than that (15.48 m^2/g) of pristine CN. Compared to pristine CN, the Zeta potential of CN-B-N$_V$ after homogeneous B doping increased slightly (Fig. S5). According to the analysis of inductively coupled plasma optical emission spectrometer (ICP-OES), the doped B atoms in CN-B-N$_V$ were estimated to be 0.18 wt% (Fig. S6).

To exploit the mechanism of B-doping-mediated N$_V$ generation, density functional theory (DFT) calculations were first carried out. The doped B would preferentially substitute the C atom of g-C$_3$N$_4$ framework along with the formation of adjacent unsaturated coordinated N species (Fig. 2a). Compared to pristine g-C$_3$N$_4$, the formation energy of N$_V$ in CN-B-N$_V$ decreased from 2.68 eV to 1.32 eV, which is conductive to the generation of N$_V$ (Fig. 2b). Experimentally, higher N$_V$ concentration in CN-B-N$_V$ than pristine CN was confirmed by the stronger signal intensity in the electron paramagnetic resonance (EPR) spectra (Fig. 2 and Fig. S7), which stemmed from the decreased formation energy of N$_V$ after B doping. Furthermore, the influence of doped B on the surface atomic arrangement of g-C$_3$N$_4$ was investigated by X-ray photoelectron spectroscopy (XPS) (Fig. S8). For CN-B-N$_V$, the peak locating at 192.1 eV in the high-resolution B 1 s spectrum stems from the formation of N-B bond (Fig. 2d). Meanwhile, a new N chemical state (397.8 eV) emerged in the N 1 s spectra, which is assigned to the formation of N-B bond (Fig. 2e) [45]. No additional B chemical states could be detected in CN-B-N$_V$. Given the spatial proximity between B and N$_V$, the formed B-N$_V$ unit on the g-C$_3$N$_4$ surface was donated as B-N$_V$ associate.

Regarding the homogeneous B doping and concomitant generation of B-N$_V$ associate, their effects on the electronic structure of CN-B-N$_V$ was subsequently investigated by DFT calculation. As revealed by the density of states (DOS), the individual N$_V$ introduced an acceptor state above the valence band (VB) maximum of CN-N$_V$, while the B-N$_V$ associate imported a new donor state below the conduction band (CB) minimum of CN-N$_V$ (Fig. 3a). The donor state composed of hybridized B 2p and C 2p orbitals decreased the bandgap of g-C$_3$N$_4$ and caused the valence band shifting towards more positive position, which are then experimentally evidenced by UV–vis absorption spectra and the valence band obtained from XPS (VB-XPS) spectra (Fig. S9). Furthermore, the influence of B-N$_V$ associate on the charge density of lowest unoccupied molecular orbital (LUMO) and highest occupied molecular orbital
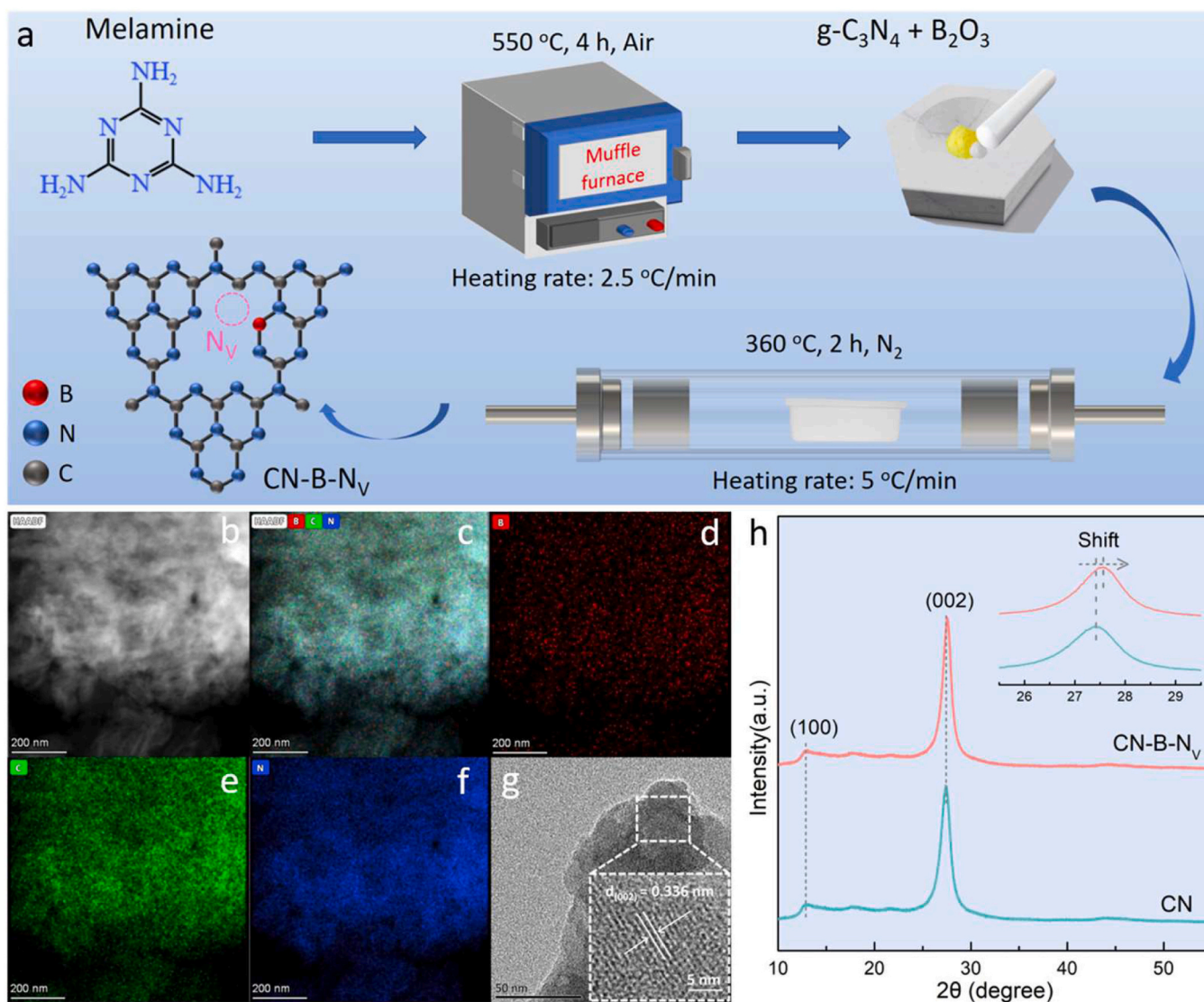
Fig. 1. Preparation of homogeneously B doped g-C_3N_4 nanosheets. (a) Schematic illustration of the synthesized sample via the molten-B_2O_3 method. (b-f) TEM image and elements mapping of B, C and N. (g) High-resolution TEM image and the corresponding SAED pattern. (h) XRD patterns of pristine and the B doped g-C_3N_4 nanosheets.

(HOMO) of g-C_3N_4 was investigated (Fig. 3b). Distinct from pristine g-C_3N_4 with uniform charge distribution in the HOMO-LUMO orbitals, the individual N_V of g-C_3N_4 causes the partially disordered energy gradient in the HOMO orbital. While the generated B-N_V associate in CN-B-N_V reconstructed the electronic structure of the HOMO-LUMO orbitals and triggered the disordered charge carriers to being localized around it.

Given the fact that robust excitonic effect in 2D layered materials originates from the strong Coulomb force within the highly ordered layered structure, the B-N_V associate with abundant localized charges intends to "break" the electronic homogeneity of g-C_3N_4 and promote excitons spontaneously dissociating into charge carriers (exciton → e^- + h^+). According to the steady-state fluorescence (PL) spectra under ambient temperature (298 K), the lower PL emission intensity of CN-B-N_V than CN suggested its higher charge separation efficiency, which is also supported by the nearly 2.5-time enhancement of photocurrent density and significantly smaller charge transfer resistance (Fig. 3c and Fig. S10). Thus, the charge carriers' lifetime of CN-B-N_V was prolonged from 8.99 ns (CN) to 12.69 ns (Fig. S11). To further clarify the effect of B-N_V associate on the excitons dissociation of g-C_3N_4, low-temperature fluorescence (PL) spectra was carried out in view of the dark features and nonradiative relaxation of excitons at room temperature [20]. At

77 K, g-C_3N_4 displayed an intensive sub-bandgap emission around 404 nm caused by the radiative decay of excitons (Fig. 3d). According to the blueshift of PL emission at room temperature (298 K) and low temperature (77 K), the exciton binding energy (E_b) of g-C_3N_4 was calculated to be 402 meV. The introduction of B-N_V associate in CN-B-N_V inhibited the strong emission peak with a less blueshift (to 443 nm), resulting in the E_b decreased to 109 meV. Therefore, homogeneous B doping induced the formation of B-N_V associate inherently weakened the excitonic effect in g-C_3N_4, further facilitating the charge carriers' separation. Restricted by the spin-forbidden characteristic of excitons under room temperature, the kinetics of excitons and charge carriers were collected by phosphorescence (PH) spectra. With a delayed time of 1 ms, pristine g-C_3N_4 showed an excitonic emission peak locating around 431 nm, corresponding to the PL spectra under room temperature (Fig. 3e). On the contrast, CN-B-N_V exhibited a largely suppressed excitonic emission but a new emission peak at 481 nm, which is ascribed to the B-N_V associate-induced emission. Combined with the electronic structure of CN-B-N_V, we speculated the corresponding photophysical process including the primary excitons' formation and latter excitons' dissociation (Fig. 3f). That is, the photoexcited electrons in the conduction band of CN-B-N_V was preferentially trapped
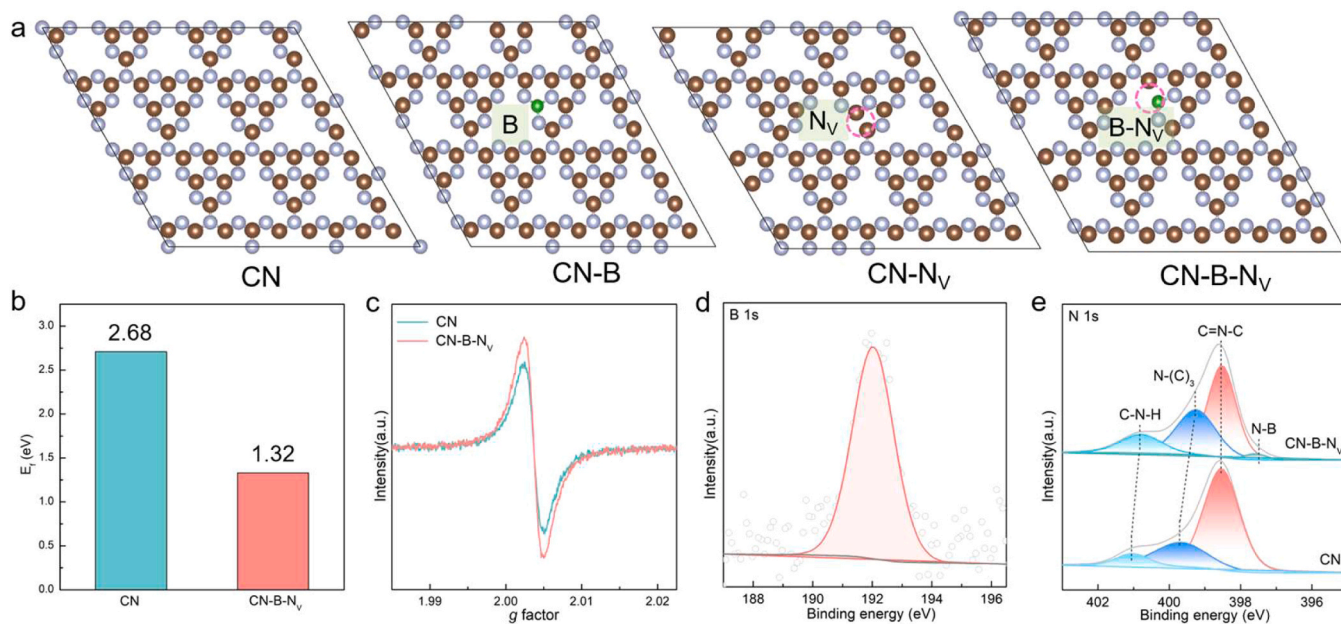
Fig. 2. Characterization of B-N$_V$ associate on CN-B-N$_V$ surface. (a) The optimized structure of CN, CN-B, CN-N$_V$ and CN-B-N$_V$. (b) The formation energy of N$_V$ of CN and CN-B-N$_V$. (c) EPR spectra of CN and CN-B-N$_V$. (d) High resolution B 1 s spectra of CN-B-N$_V$. (e) High resolution N 1 s spectra of CN and CN-B-N$_V$.
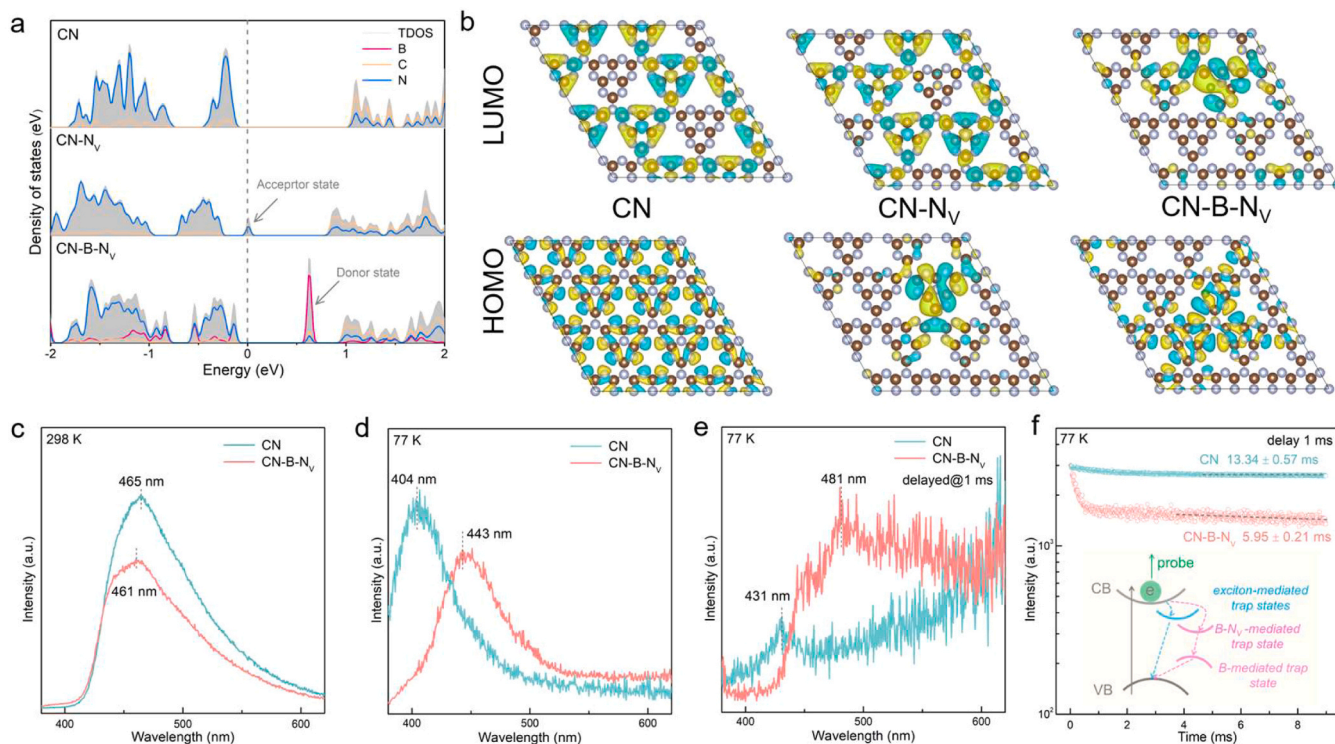
Fig. 3. Behaviours of charge carriers′ kinetics. (a) Calculated DOS of CN, CN-N$_V$ and CN-B-N$_V$. (b) Charge density profile of HOMO and LUMO orbitals for CN, CN-N$_V$ and CN-B-N$_V$. The yellow and blue isosurfaces represent charge accumulation and depletion in the space, respectively. (c) Room-temperature steady-state PL spectra (298 K), (d) low-temperature steady-state PL spectra (77 K), (e) low-temperature steady-state PH spectra (77 K), and (f) low-temperature time-resolved PH spectra (77 K) of CN and CN-B-N$_V$. The inset in (f) is the schematic illustration of excitons dissociation and free charge carrier generation in CN-B-N$_V$.

by the deeper B-N$_V$-mediated trap state rather than the shallow exciton-mediated trap state owing to the weakened excitonic effect, thus avoiding exciton formation. Furthermore, the relaxed photoelectrons were trapped again by the B-mediated trap state before them recombining with holes, further supressing the rapid recombination of electrons and holes. As revealed by the time-resolved PH spectra, CN-B-N$_V$

had a much shorter exciton decay lifetime (5.95 ms) than that of pristine g-C$_3$N$_4$ (13.34 ms). These results manifested that the homogeneous B doping-mediated B-N$_V$ associate generated in g-C$_3$N$_4$ indeed favors of exciton dissociation into charge carriers with a prominently prolonged lifetime.

In view of the B doping-induced exciton dissociation in g-C$_3$N$_4$, the

energy-transfer-dominated O_2 activation process might be suppressed. According to EPR spectra, a triplet-peak signal (1:1:1, $\alpha_N = 16.9$ G) of $^1O_2$ emerged in the g-C_3N_4 system with the addition of 2,2,6,6-tetramethyl-4-piperidinol-N-oxyl (TEMP) as the trapping agent (Fig. 4a). However, the EPR signal of $^1O_2$ of CN-B-N_V reduced remarkably, suggesting the weakened excitonic effect. Meanwhile, the generation of $\bullet O_2^-$ was verified by the oxidation of 5,5-dimethyl-1-pyrroline N-oxide (DMPO). Intriguingly, CN-B-N_V displayed an intensive signal of DMPO-$\bullet O_2^-$ adduct ($\alpha_N = 12.9$ G, $\alpha_H = 10.3$ G) than that of CN (Fig. 4b). As aforementioned, the $\bullet O_2^-$ generation is governed by 2e$^-$ ORR process. The higher $\bullet O_2^-$ activation selectivity over CN-B-N_V suggests its superior potential to boost excitons dissociation into charge carriers. Furthermore, the charge carrier-involved O_2 activation toward H_2O_2 production over CN-B-N_V might be promoted substantially. Given that H_2O_2 photosynthesis highly depends on the available O_2 molecules on catalyst's surface, the capacity of samples for O_2 adsorption and activation was then characterized by the O_2-temperature programmed desorption (O_2-TPD). The larger integral area of CN-B-N_V suggested its more surface sites to bond with O_2 (Fig. 4c). While the higher desorption temperature of CN-B-N_V (168 °C) than CN (137 °C) indicated its stronger O_2 activation capacity. To this end, the photocatalytic performance of CN-B-N_V nanosheets for H_2O_2 production was systematically evaluated (Fig. S12). A series of control experiments demonstrated that catalysts, light and O_2 are essential factors for H_2O_2 photosynthesis. Under the optimized conditions, the H_2O_2 yield over CN-B-N_V in isopropanol (IPA, a hole scavenger) solution within a reaction period (150 min) reached up to 352.6 μmol L^{-1}, which is 4.2-fold increase than that in pure water (Fig. 4d and Fig. S13-S15). After being normalized with the specific surface area, the H_2O_2 yield of CN-B-N_V is still higher than that of pristine g-C_3N_4 (Fig. 4e). CN-B-N_V exhibited excellent photostability for continuous H_2O_2 production without obvious decay within ten cycles running, which is also supported by the almost unchanged crystalline, morphology and N_V concentration (Fig. 4f and Fig. S16). Compared with other g-C_3N_4-based photocatalysts, the CN-B-N_V featurig with B-N_V associates exhibited superior H_2O_2 yield under visible light (Table S1). This crafted CN-B-N_V photocatalyst can also produce H_2O_2 in the water from Yellow River under visible light with a yield of 89.8 μmol L^{-1} (Fig. S17). More importantly, the CN-B-N_V displayed a superior tolerance toward different environmental ions, such as Na$^+$, K$^+$, Cl$^-$, SO$_4^{2-}$, for visible-light-driven H_2O_2 production (Fig. S18).

To investigate whether the detected H_2O_2 generated from the 2e$^-$ ORR or 2e$^-$ WOR pathways, different scavengers were used to trap the reactive species (e$^-$: K$_2$Cr$_2$O$_7$; h$^+$: EDTA-2Na; $\bullet O_2^-$: p-benzoquinone (p-BQ); $^1O_2$: L-Tryptophan) (Fig. 4g). After the e$^-$ and $\bullet O_2^-$ being captured, the H_2O_2 production of CN-B-N_V was prominently inhibited. On the contrary, the H_2O_2 yield increased slightly when the h$^+$ was trapped by EDTA-2Na. No obvious photoactivity decay was observed with the addition of L-Tryptophan, excluding the contribution of $^1O_2$ to H_2O_2
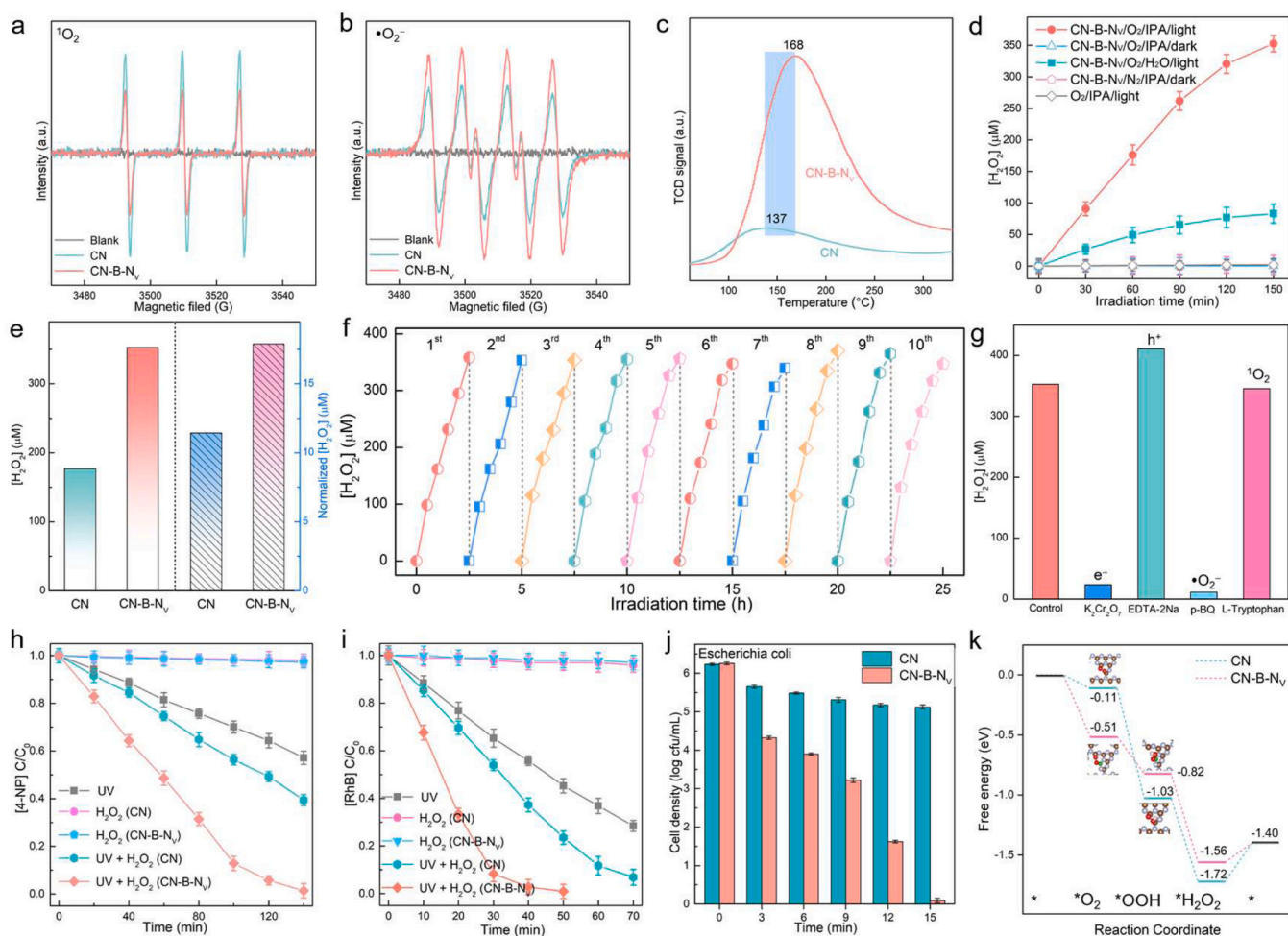
Fig. 4. Visible light-driven H_2O_2 photosynthesis. EPR spectra for (a) TEMP-$^1O_2$ and (b) DMPO-$\bullet O_2^-$ adducts over CN and CN-B-N_V under visible light. (c) O_2-TPD profiles of CN and CN-B-N_V. (d) Photocatalytic H_2O_2 production over CN-B-N_V under different reaction conditions. (e) Comparison of H_2O_2 yields over CN and CN-B-N_V. (f) Cycling tests of photocatalytic H_2O_2 production over CN-B-N_V in the IPA solution under visible light. (g) The H_2O_2 yield over CN-B-N_V with or without adding of different scavengers. (h-i) On-site utilization of the produced H_2O_2 for degradation of 4-NP and RhB. (j) On-site sterilization of *Escherichia coil* by the produced H_2O_2. (k) Gibbs free energy (ΔG) diagram of H_2O_2 production over CN and CN-B-N_V. *indicates surface adsorption state.

formation[6]. All these results manifested that the $2e^-$ ORR is responsible for the high-efficiency H_2O_2 production of CN-B-N_V. As a common oxidant, H_2O_2 is widely used in organic wastewater treatment and sterilization [25,46,47]. Compared to the individual ultraviolet light irradiation or pristine CN, the on-site generated H_2O_2 by CN-B-N_V showed a much higher degradation efficiency for para-chloronitrobenzene (4-NP, a representative of chemical raw material and intermediate with high toxicity), Rhodamine B (RhB, a representative of synthetic dye), tetracycline (TC, a representative of antibiotic), bisphenol A (BPA, a representative of hormone drug) and 4-chlorophenol (4-CP, a precursor of dyes and drugs) (Fig. 4h-i and Fig. S19-S20), suggesting its superior versatility to degrade different organic contaminants. For the typical bacteria in drinking water (≈ 6.2 logCFU mL^{-1} *Escherichia coli*), its growth was completely inhibited within 15 min after adding the produced H_2O_2 solution (Fig. 4j and Fig. S21). These results suggested that the solar light-driven H_2O_2 synthesis of CN-B-N_V is promising for the organic wastewater purification and drinking water sterilization.

Based on the above results and discussion, the mechanism of $2e^-$ ORR-driven H_2O_2 production can be understood. First, the adsorbed O_2 on catalysts' surface was directly reduced by photogenerated electrons to form $\bullet O_2^-$. Subsequently, the newly generated $\bullet O_2^-$ would react with protons, stemming from the dissociation of water molecule or the oxidation of EG, to produce H_2O_2, which then diffuses into the solution phase. Undoubtably, the efficient adsorption and activation of O_2 on catalysts' surface was the prerequisite step for the $2e^-$ ORR-driven H_2O_2 photosynthesis. According to the calculated Gibbs free energy of photocatalysts and active intermediates, the adsorption energy of O_2 on the B-N_V associate of CN-B-N_V (-0.51 eV) is much larger than that (-0.11 eV) of CN (Fig. 4k and Fig. S22). Benefiting from the lower $\pi * 2p$ orbital, the adsorbed O_2 was activated into $\bullet O_2^-$ in a terminal side-on mode by the localized photoelectrons in the B-N_V associate, which is supported by the calculation of Bader charge (Fig. S23). Throughout the whole $2e^-$ ORR pathway ($* + O_2 \rightarrow *O_2 \rightarrow *OOH \rightarrow *H_2O_2 \rightarrow * + H_2O_2$), the desorption of $*H_2O_2$ from catalysts' surface is the rate-determining step because it needs extra energy to overcome the uphill barrier [6]. Distinct from pristine g-C$_3$N$_4$ ($+0.32$ eV), the energy barrier of $*H_2O_2$ desorption from the CN-B-N_V surface is about $+0.16$ eV, suggesting the B-N_V associate is more beneficial to H_2O_2 photosynthesis via the $2e^-$ ORR pathway.

4. Conclusion

In conclusion, we have demonstrated the homogeneously B doped CN-B-N_V nanosheet synthesized through a B$_2$O$_3$ molten-salt-based strategy enables to realize efficient $2e^-$ ORR-driven H_2O_2 photosynthesis and apply to *on site* wastewater purification. The doped B atoms in the g-C$_3$N$_4$ framework weakened the robust excitonic effect and boosted excitons dissociating into charge carriers, whereas the B-N_V associates originating from the B doping-mediated N_V generation spontaneously promoted the adsorption and activation of O_2, as well as the H_2O_2 desorption. Benefiting from these two virtues, CN-B-N_V exhibited a superior photoactivity for $2e^-$ ORR-driven H_2O_2 production with a yield of 182 μmol h^{-1} and selectivity of $\approx 100\%$. The produced H_2O_2 could degrade different organic wastewater (4-NP, RhB, TC, BPA and 4-CP) and kill *Escherichia coil* in drinking water effectively. This work presents a green and safe way for artificial H_2O_2 production and *on site* wastewater purification.

CRediT authorship contribution statement

Fanyu Wang: Visualization, Validation, Methodology. **Yanbiao Shi:** Writing – review & editing, Writing – original draft, Software, Project administration, Funding acquisition. **Haobo Zhang:** Visualization, Validation, Methodology, Formal analysis, Data curation. **Zhiying Wang:** Visualization, Validation, Methodology, Formal analysis, Data curation **Longhui Zheng:** Writing – review & editing, Writing – original draft, Project administration, Methodology, Investigation, Funding acquisition, Formal analysis, Data curation. **Qizhao Wang:** Writing – review & editing, Resources, Project administration, Funding acquisition, Conceptualization. **Jiahui Yue:** Visualization, Validation, Methodology, Formal analysis, Data curation, Conceptualization. **Di Lin:** Writing – original draft, Visualization, Validation, Methodology, Formal analysis, Data curation. **Zhongsen Wang:** Visualization, Validation, Software, Methodology, Formal analysis, Data curation.

Declaration of Competing Interest

Data availability

Data will be made available on request.

Acknowledgements

Appendix A. Supporting information

Supplementary data associated with this article can be found in the online version at doi:10.1016/j.apcatb.2024.123811.

References

[1] R.J. Lewis, K. Ueura, X. Liu, Y. Fukuta, T.E. Davies, D.J. Morgan, L. Chen, J. Qi, J. Singleton, J.K. Edwards, S.J. Freakley, C.J. Kiely, Y. Yamamoto, G.J. Hutchings, Highly efficient catalytic production of oximes from ketones using in situ-generated H$_2$O$_2$, Science 376 (2022) 615–620.

[2] X. Shi, S. Back, T.M. Gill, S. Siahrostami, X. Zheng, Electrochemical synthesis of H$_2$O$_2$ by two-electron water oxidation reaction, Chem 7 (2021) 38–63.

[3] D. Chen, W. Chen, Y. Wu, L. Wang, X. Wu, H. Xu, L. Chen, Covalent organic frameworks containing dual O$_2$ reduction centers for overall photosynthetic hydrogen peroxide production, Angew. Chem. Int. Ed. 62 (2023) e202217479.

[4] Z. Li, Y. Zhou, Y. Zhou, K. Wang, Y. Yun, S. Chen, W. Jiao, L. Chen, B. Zou, M. Zhu, Dipole field in nitrogen-enriched carbon nitride with external forces to boost the artificial photosynthesis of hydrogen peroxide, Nat. Commun. 14 (2023) 5742.

[5] P. Zhang, Y. Tong, Y. Liu, J.J.M. Vequizo, H. Sun, C. Yang, A. Yamakata, F. Fan, W. Lin, X. Wang, W. Choi, Heteroatom dopants promote two-electron O$_2$ reduction for photocatalytic production of H$_2$O$_2$ on polymeric carbon nitride, Angew. Chem. Int. Ed. 59 (2020) 16209–16217.

[6] J. Luo, X. Wei, Y. Qiao, C. Wu, L. Li, L. Chen, J. Shi, Photoredox-promoted co-production of dihydroisoquinoline and H$_2$O$_2$ over defective Zn$_3$In$_2$S$_6$, Adv. Mater. 35 (2023) 2210110.

[7] P. Ren, T. Zhang, N. Jain, H.Y.V. Ching, A. Jaworski, G. Barcaro, S. Monti, J. Silvestre-Albero, V. Celorrio, L. Chouhan, A. Rokicińska, E. Debroye, P. Kuśtrowski, S. Van Doorslaer, S. Van Aert, S. Bals, S. Das, An atomically dispersed Mn-photocatalyst for generating hydrogen peroxide from seawater via the water oxidation reaction (WOR), J. Am. Chem. Soc. 15 (2023) 16584–16596.

[8] T. Liu, Z. Pan, J.J.M. Vequizo, K. Kato, B. Wu, A. Yamakata, K. Katayama, B. Chen, C. Chu, K. Domen, A general interfacial-energetics-tuning strategy for enhanced artificial photosynthesis, Nat. Commun. 13 (2022) 1034.

[9] F. Liu, P. Zhou, Y. Hou, H. Tan, Y. Liang, J. Liang, Q. Zhang, S. Guo, M. Tong, J. Ni, Covalent organic frameworks for direct photosynthesis of hydrogen peroxide from water, air and sunlight, Nat. Commun. 14 (2023) 4344.

[10] Y. Zhang, C. Pan, G. Bian, J. Xu, Y. Dong, Y. Zhang, Y. Lou, W. Liu, Y. Zhu, H_2O_2 generation from O_2 and H_2O on a near-infrared absorbing porphyrin supramolecular photocatalyst, Nat. Energy 8 (2023) 361–371.

[11] H. Li, H. Zhu, Y. Shi, H. Shang, L. Zhang, J. Wang, Vacancy-rich and porous NiFe-layered double hydroxide ultrathin nanosheets for efficient photocatalytic NO oxidation and storage, Environ. Sci. Technol. 56 (2022) 1771–1779.

[12] Y. Chen, S. Guan, H. Ge, X. Chen, Z. Xu, Y. Yue, H. Yamashita, H. Yu, H. Li, Z. Bian, Photocatalytic dissolution of precious metals by TiO_2 through photogenerated free radicals, Angew. Chem. Int. Ed. 61 (2022) e202213640.

[13] J. Zhang, J. Lang, Y. Wei, Q. Zheng, L. Liu, Y.-H. Hu, B. Zhou, C. Yuan, M. Long, Efficient photocatalytic H_2O_2 production from oxygen and pure water over graphitic carbon nitride decorated by oxidative red phosphorus, Appl. Catal. B Environ. 298 (2021) 120522.

[14] Z. Yang, Y. Shi, H. Li, C. Mao, X. Wang, X. Liu, X. Liu, L. Zhang, Oxygen and chlorine dual vacancies enable photocatalytic O_2 dissociation into monatomic reactive oxygen on BiOCl for refractory aromatic pollutant removal, Environ. Sci. Technol. 56 (2022) 3587–3595.

[15] X. Xu, J. Wang, T. Chen, N. Yang, S. Wang, X. Ding, H. Chen, Deep insight into ROS mediated direct and hydroxylated dichlorination process for efficient photocatalytic sodium pentachlorophenate mineralization, Appl. Catal. B Environ. 296 (2021) 120352.

[16] X. Chen, S. Guan, J. Zhou, H. Shang, J. Zhang, F. Lv, H. Yu, H. Li, Z. Bian, Photocatalytic free radical-controlled synthesis of high-performance single-atom catalysts, Angew. Chem. Int. Ed. 62 (2023) e202212734.

[17] C. Chu, Q. Zhu, Z. Pan, S. Gupta, D. Huang, Y. Du, S. Weon, Y. Wu, C. Muhich, E. Stavitski, K. Domen, J.-H. Kim, Spatially separating redox centers on 2D carbon nitride with cobalt single atom for photocatalytic H_2O_2 production, Proc. Natl. Acad. Sci. 117 (2020) 6376–6382.

[18] H. Tan, P. Zhou, M. Liu, Q. Zhang, F. Liu, H. Guo, Y. Zhou, Y. Chen, L. Zeng, L. Gu, Z. Zheng, M. Tong, S. Guo, Photocatalysis of water into hydrogen peroxide over an atomic Ga-N_5 site, Nat. Synth. 2 (2023) 557–563.

[19] J. Liu, Y. Liu, N. Liu, Y. Han, X. Zhang, H. Huang, Y. Lifshitz, S.-T. Lee, J. Zhong, Z. Kang, Metal-free efficient photocatalyst for stable visible water splitting via a two-electron pathway, Science 347 (2015) 970–974.

[20] D. Wei, Y. Tan, Y. Wang, T. Kong, S. Shen, S.S. Mao, Function-switchable metal/semiconductor junction enables efficient photocatalytic overall water splitting with selective water oxidation products, Sci. Bull. 65 (2020) 1389–1395.

[21] H. Dotan, K. Sivula, M. Grätzel, A. Rothschild, S.C. Warren, Probing the photoelectrochemical properties of hematite (α-Fe_2O_3) electrodes using hydrogen peroxide as a hole scavenger, Energy Environ. Sci. 4 (2011) 958–964.

[22] Q. Li, Y. Jiao, Y. Tang, J. Zhou, B. Wu, B. Jiang, H. Fu, Shear stress triggers ultrathin-nanosheet carbon nitride assembly for photocatalytic H_2O_2 production coupled with selective alcohol oxidation, J. Am. Chem. Soc. 145 (2023) 20837–20848.

[23] Z. Teng, Q. Zhang, H. Yang, K. Kato, W. Yang, Y.-R. Lu, S. Liu, C. Wang, A. Yamakata, C. Su, B. Liu, T. Ohno, Atomically dispersed antimony on carbon nitride for the artificial photosynthesis of hydrogen peroxide, Nat. Catal. 4 (2021) 374–384.

[24] Y. Chen, M. Xu, J. Wen, Y. Wan, Q. Zhao, X. Cao, Y. Ding, Z.L. Wang, H. Li, Z. Bian, Selective recovery of precious metals through photocatalysis, Nat. Sustain. 4 (2021) 618–626.

[25] L.-J. Sun, H.-W. Su, Q.-Q. Liu, J. Hu, L.-L. Wang, H. Tang, A review on photocatalytic systems capable of synchronously utilizing photogenerated electrons and holes, Rare Met. 41 (2022) 2387–2404.

[26] H. Song, L. Wei, C. Chen, C. Wen, F. Han, Photocatalytic production of H_2O_2 and its in situ utilization over atomic-scale Au modified MoS_2 nanosheets, J. Catal. 376 (2019) 198–208.

[27] A. Gopakumar, P. Ren, J. Chen, B.V. Manzolli Rodrigues, H.Y. Vincent Ching, A. Jaworski, S.V. Doorslaer, A. Rokicińska, P. Kuśtrowski, G. Barcaro, S. Monti, A. Slabon, S. Das, Lignin-supported heterogeneous photocatalyst for the direct generation of H_2O_2 from seawater, J. Am. Chem. Soc. 144 (2022) 2603–2613.

[28] Y.-X. Li, W. Choi, Polarization-induced exciton dissociation in COF photocatalyst, Chem. Catal. 2 (2022) 1517–1519.

[29] Y. Guo, Q. Zhou, J. Nan, W. Shi, F. Cui, Y. Zhu, Perylenetetracarboxylic acid nanosheets with internal electric fields and anisotropic charge migration for photocatalytic hydrogen evolution, Nat. Commun. 13 (2022) 2067.

[30] Y. Zhao, S. Zhang, R. Shi, G.I.N. Waterhouse, J. Tang, T. Zhang, Two-dimensional photocatalyst design: a critical review of recent experimental and computational advances, Mater. Today 34 (2020) 78–91.

[31] A. Rogolino, I.F. Silva, N.V. Tarakina, M.A.R. da Silva, G.F.S.R. Rocha, M. Antonietti, I.F. Teixeira, Modified poly(heptazine imides): minimizing H_2O_2 decomposition to maximize oxygen reduction, ACS Appl. Mater. Interfaces 14 (2022) 49820–49829.

[32] Y. Shi, H. Li, C. Mao, G. Zhan, Z. Yang, C. Ling, K. Wei, X. Liu, Z. Ai, L. Zhang, Manipulating excitonic effects in layered bismuth oxyhalides for photocatalysis, ACS EST Eng. 2 (2022) 957–974.

[33] Y. Shi, Z. Yang, L. Shi, H. Li, X. Liu, X. Zhang, J. Cheng, C. Liang, S. Cao, F. Guo, X. Liu, Z. Ai, L. Zhang, Surface boronizing can weaken the excitonic effects of BiOBr nanosheets for efficient O_2 activation and selective NO oxidation under visible light irradiation, Environ. Sci. Technol. 56 (2022) 14478–14486.

[34] H. Wang, D. Yong, S. Chen, S. Jiang, X. Zhang, W. Shao, Q. Zhang, W. Yan, B. Pan, Y. Xie, Oxygen-vacancy-mediated exciton dissociation in BiOBr for boosting charge-carrier-involved molecular oxygen activation, J. Am. Chem. Soc. 140 (2018) 1760–1766.

[35] Y. Shi, G. Zhan, H. Li, X. Wang, X. Liu, L. Shi, K. Wei, C. Ling, Z. Li, H. Wang, C. Mao, X. Liu, L. Zhang, Simultaneous manipulation of bulk excitons and surface defects for ultrastable and highly selective CO_2 photoreduction, Adv. Mater. 33 (2021) 2100143.

[36] G. Zhang, Y. Xu, D. Yan, C. He, Y. Li, X. Ren, P. Zhang, H. Mi, Construction of K^+ ion gradient in crystalline carbon nitride to accelerate exciton dissociation and charge separation for visible light H_2 production, ACS Catal. 11 (2021) 6995–7005.

[37] Y. Shi, H. Shou, H. Li, G. Zhan, X. Liu, Z. Yang, C. Mao, J. Cheng, X. Zhang, Y. Jiang, S. Zhao, J. Wang, X. Liu, L. Song, H. Sun, L. Zhang, Visible light-driven conversion of carbon-sequestrated seawater into stoichiometric CO and HClO with nitrogen-doped BiOCl atomic layers, Angew. Chem. Int. Ed. 62 (2023) e202302286.

[38] Y. Shi, J. Li, C. Mao, S. Liu, X. Wang, X. Liu, S. Zhao, X. Liu, Y. Huang, L. Zhang, Van der Waals gap-rich BiOCl atomic layers realizing efficient, pure-water CO_2-to-CO photocatalysis, Nat. Commun. 12 (2021) 5923.

[39] H. Wang, X. Sun, D. Li, X. Zhang, S. Chen, W. Shao, Y. Tian, Y. Xie, Boosting hot-electron generation: exciton dissociation at the order–disorder interfaces in polymeric photocatalysts, J. Am. Chem. Soc. 139 (2017) 2468–2473.

[40] L. Yu, H. Li, H. Shang, P. Xing, B. Zhou, Z. Chen, X. Liu, H. Zhang, Y. Shi, L. Zhang, Locally asymmetric BiOBr for efficient exciton dissociation and selective O_2 activation toward oxidative coupling of amines, ACS Nano 17 (2023) 15077–15084.

[41] Y. Shi, C. Zhang, Z. Yang, X. Liu, X. Zhang, C. Ling, J. Cheng, C. Liang, C. Mao, L. Zhang, Interfacial electrostatic field boosted exciton dissociation of phosphorylated BiOBr for efficient O_2 activation and chlorobenzene degradation, J. Phys. Chem. C 126 (2022) 21847–21856.

[42] H. Wang, S. Jiang, W. Liu, X. Zhang, Q. Zhang, Y. Luo, Y. Xie, Ketones as molecular co-catalysts for boosting exciton-based photocatalytic molecular oxygen activation, Angew. Chem. Int. Ed. 59 (2020) 11093–11100.

[43] Y. Shi, Z. Yang, Y. Liu, J. Yu, F. Wang, J. Tong, B. Su, Q. Wang, Fabricating a g-C_3N_4/CuO_x heterostructure with tunable valence transition for enhanced photocatalytic activity, RSC Adv. 6 (2016) 39774–39783.

[44] Y. Kang, Y. Yang, L.-C. Yin, X. Kang, G. Liu, H.-M. Cheng, An amorphous carbon nitride photocatalyst with greatly extended visible-light-responsive range for photocatalytic hydrogen generation, Adv. Mater. 27 (2015) 4572–4577.

[45] G. Liu, C. Sun, L. Cheng, Y. Jin, H. Lu, L. Wang, S.C. Smith, G.Q. Lu, H.-M. Cheng, Efficient promotion of anatase TiO_2 photocatalysis via bifunctional surface-terminating Ti–O–B–N structures, J. Phys. Chem. C 113 (2009) 12317–12324.

[46] Y. Shi, X. Wang, X. Liu, C. Ling, W. Shen, L. Zhang, Visible light promoted Fe_3S_4 Fenton oxidation of atrazine, Appl. Catal. B Environ. 277 (2020) 119229.

[47] Q. Lian, Z. Liang, X. Guan, Z. Tang, R. Zhang, B. Yang, Y. Wu, H. Zhao, C. He, D. Xia, High-coordinated Bi^V/Bi^{IV} regulates photocatalytic selective activation of structural oxygen and self-generated H_2O_2 dominating an efficient synergistic sterilization, Appl. Catal. B Environ. 331 (2023) 122724.